WILEY | Hindawi

Research Article

Investigation into Macro- and Microcrack Propagation Mechanism of Red Sandstone under Different Confining Pressures Using 3D Numerical Simulation and CT Verification

Wen Zhang (ID)**, Yan-yu Chen** (ID)**, Jin-ping Guo** (ID)**, Sai-sai Wu** (ID)**, and Cheng-yuan Yan** (ID)

School of Resources Engineering, Xi'an University of Architecture and Technology, Xi'an 710055, China

Correspondence should be addressed to Wen Zhang; zhangwen@xauat.edu.cn and Sai-sai Wu; saisai.wu@xauat.edu.cn

The growth and evolvement features of crack are of great significance to study the failure mechanism of rock mass and valuate the stability of the cavity. In this study, in order to obtain the mechanics parameters and external macroscopic crack propagation characteristics of red sandstone, triaxial compression tests were carried out. Based on the experimental results, a numerical model was established through the reasonable parameter calibration by the PFC^{3D} software. The internal and external crack propagation processes of red sandstone under triaxial compression were simulated. Moreover, to verify the simulation results, the CT scanning and three-dimensional reconstruction technologies were used to observe the internal crack state of the specimens. The results showed that the internal crack failures occurred first at the end of the rock specimen. Then, the microcracks continued to accumulate and expand under the combined action of axial stress and confining pressure. The accumulated microcracks finally converged to form a macroscopic oblique shear failure. Based on the homogenizing treatment and reasonable parameter calibration, the internal and external crack expansion and evolution processes of the rock were simulated by the PFC^{3D} model and the simulation results are consistent with the results obtained from the triaxial compression test and the CT scanning. The macro- and microfailure mode of crack propagation of the specimen deepens the understanding of rock failure mechanism. The PFC^{3D} homogenization simulation method provides a new feasible method to study the macro- and microfailure mode of internal and external crack propagation of rock under compression.

1. Introduction

The rock mass is an anisotropic heterogeneous body formed by one or more rock-forming minerals in a certain combination that contains structural defects such as cracks and joints. The composition of rock minerals, combination mode, and development degree of cracks and joints determine the physical and mechanical properties of the rock [1–7]. In the ore excavation process, the rock mass is subjected to complex loading and unloading stress processes, which leads to the deformation and destruction of the rock mass. The distribution and expansion of its fissures directly affect mining safety, such as underground water inrush and roof failure which are all developed and evolved from cracks and other weak surfaces [8, 9]. In underground mining, the development of fissures is one of the major causes leading to the destruction

of rock projects [10–12]. Understanding the crack propagation mechanism can provide a feasible basis for engineering safety design. Effective monitoring methods can identify the distribution and expansion of cracks in rock masses for safety early warning, which help achieve safe and efficient mining.

The expansion and evolution of fissures have long been a hot issue of concern to researchers all around the world [13–15]. The laboratorial examination is one of the commonly used methods to study the fissure behavior of rock mass. Mokhtarian et al. used the filling material to simulate the rock and studied its weak plane failure under triaxial compression [16]. Yang et al. studied the strength and failure characteristics of red sandstone by the triaxial compression test [17]. Ma et al. investigated the effects of temperature on granite failure characteristics through high-temperature triaxial tests [18]. Jiang et al. analyzed both the uniaxial

compressive and triaxial compressive strength of sandstone under air-drying, natural, and saturation conditions [19]. Most of the studies above focused on rock mechanical properties and failure characteristics under triaxial action, but only few studies investigated the mechanism of the internal crack prorogation and expansion.

CT scanning technology can accurately characterize the internal fractures of the rock. Kawakata et al. used the X-ray CT scanning system to study the fracture process of granite under different load conditions [20]. Christe et al. evaluated the degree of alteration of highly tectonized carbonate rock specimens based on X-ray computed tomography and led to a diagnosis of alteration which appeared objective, precise, and in agreement with the visual observations [21]. Yang et al. investigated the failure mechanism of transversely isotropic composite rock-like material on the microlevel by CT, and the 3D volume renders were in good agreement with the actual surface crack photographs of specimens [22]. Zhu et al. simulated and predicted the mechanical properties and fracture characteristics of the rock based on the CT three-dimensional numerical simulation [23]. CT scanning technology can respond to changes in the rock specimen's internal fractures in a nondestructive and multi-directional manner, but the expense is high and the current measurement sample size is small, which cannot meet the research of large-size specimens.

Because of its convenience and accuracy, the numerical simulation methods were used by many researchers to study rock behaviors [24–26]. Fan et al. established the bonded particle models containing flaws or/and openings in order to investigate the mechanical properties as well as the crack propagation characteristics of the rock under uniaxial compression [27]. Wu et al. used PFC to simulate rocks with different cavities and fissures and found three rock bridge coalescence modes: tensile, shear, and tensile-shear modes [28]. Zhang et al. studied the cracking process in rock-like material containing a single flaw by PFC^{2D} and found that the numerical simulation could reproduce the indoor test phenomenon [29]. It is worth noting that two-dimensional numerical simulation is a plane stress model, which is easier to limit the boundary conditions and apply the loads, but it is quite different from the actual model. In order to establish a numerical model consisting with the actual simulation, Yang et al. introduced the establishment of a three-dimensional model of agglomerated particles and pores based on CT scanning [30]. Zhao used CT reconstruction technology to compare the PFC^{2D} and PFC^{3D} models and found that the internal structure built in 3D is more complete, which showed more realistic macromechanical behavior and deformation patterns [31]. The consistency between the three-dimensional simulation and the actual model determines that the simulation results are closer to the real macromechanical behavior, which is more conducive to the study of the development of macro- and microfissures inside the specimen.

To reveal the crack evolution process of red sandstone, triaxial compression tests on red sandstone under different confining pressures were carried out to obtain the mechanical parameters and failure characteristics. The typical red sandstone specimen was scanned by CT experiment after failure to obtain each scan layer CT image, and AVIZO software was used to reconstruct the CT images in three dimensions. Based on homogenization processing, the deformation and failure models of red sandstone were established by PFC^{3D} software. The macro- and microcrack failure characteristics and processes under different confining pressures were simulated. Through the comparison of the results obtained from laboratory tests, CT images, and PFC^{3D} simulations, the feasibility of the PFC^{3D} model to study the crack propagation characteristics of the rock specimen was verified. The proposed methodologies and the obtained results provide a new method for the study of rock mechanical properties and damage mechanisms.

2. Experiment

2.1. Material Preparation. The rock specimens used in the tests are red sandstone, and all the specimens were taken from the same rock. The specimen's homogeneity is good, which reduces the influence of the dispersion of the specimens on the experimental results. The specimens were prepared according to the standards of the "International Society of Rock Mechanics" and cut into standard cylindrical specimens with a diameter of 50 mm and a height of 100 mm.

2.2. Experimental Procedures. The triaxial compression test and CT scan test were carried out on the prepared red sandstone specimens.

2.2.1. Triaxial Compression Test. The SAM-2000 testing machine was used to perform triaxial compression experiments on the specimens (Figure 1). The red sandstone specimens were tested under confining pressures of 5, 10, 15, and 20 MPa. The stress-strain curves and deformation parameters of the rock specimens under different confining pressures were obtained, which provided basic data to study the crack propagation laws and conduct the numerical simulations.

2.2.2. CT Scan Test. The MS-Voxel450 CT scanner (Figure 2(a)) was used to perform CT scanning analysis on the red sandstone specimen to study the inner fracture expansion after the triaxial test.

The CT scanning system principle is based on the different X-ray absorption capabilities of the different materials when X-rays penetrate through the materials (Figure 2(b)). When X-rays pass through an object, part of the X-ray energy is absorbed and the X-rays are attenuated. The unabsorbed X-rays pass through the test material and reach the detector. The detector converts the received X-ray energy into electrical signals, which are digitized by the computer.

3. Triaxial Test Results and Deformation Characteristic Analysis

3.1. Triaxial Test Results and Analysis. In order to reduce the influence of temperature on the test results, the laboratory temperature was strictly controlled at $20(\pm0.5)^{\circ}C$ during the tests. The basic mechanical parameters and the
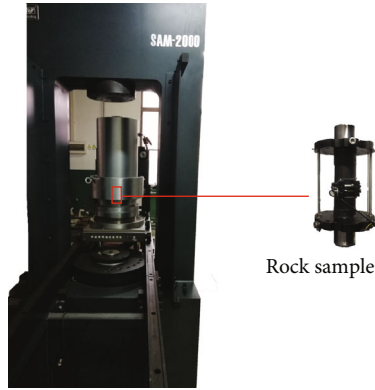
Figure 1: SAM-2000 triaxial testing machine.

corresponding stress-strain curves of red sandstone under different confining pressures were obtained, as shown in Table 1 and Figure 3.

From Figure 3(a), it can be seen that the stress-strain curves of red sandstone specimens under different confining pressures can be roughly divided into four stages. The stages are described as the elastic deformation stage, microcrack stable propagation stage, microcrack unstable propagation stage, and the postfailure stage (Figure 3(b)). The characteristics of each stage are described in detail as follows: (1) The elastic deformation stage. The curve is approximately a straight line; the rock undergoes elastic deformation. The strain continues to increase, and no new cracks are generated in this stage. If the load is unloaded at this stage, the strain can be restored. (2) The stage in which microcracks bifurcate and expand stably. The microcracks inside the rock sample begin to branch, expand, or generate new microcracks under the action of axial force. In this stage, the microcracks stop to expand once the load stops increasing. (3) The stage that the microcracks are expanding unstably. The stress at point II is the yield stress. When the stress value exceeds point II, even if the load stops increasing, the microcracks are unceasingly expanding, and this stress-strain curve presents a concave shape. (4) The postfailure stage. The macroscopic failure occurs at point III. As the strain increases, the rock continues to fail, and microcracks continue to penetrate to form a macroscopic fracture plane, and the bearing capacity of the rock decreased, until point IV, the rock broke completely. The stresses σ_I, σ_{II}, σ_{III}, and σ_{IV} correspond to four stages, which are called the elastic limit, yield stress, peak value of strength, and residual strength of rock, respectively.

At the same time, Figure 3(a) can also clearly reflect that the rock specimen's peak strength increases as the confining pressure increases, but the increments are gradually decreasing. At the confining pressures of 5, 10, 15, and 20 MPa, the maximum axial stresses are 59.70, 80.99, 98.21, and 110.12 MPa, respectively. For every additional 5 MPa increasing in confining pressure, the value of maximum axial stress of red sandstone increases by 21.29, 17.22, and 11.91 MPa. The axial strain at the peak increases with the increase of confining pressure. When the confining pressure is 5 MPa, the axial strain at the peak is 0.76×10^{-2}. For each 5 MPa

increase in the confining pressure, the axial strain at the peak increases to 0.92×10^{-2}, 1.27×10^{-2}, and 1.41×10^{-2}. The slope of the elastic phase in the stress-strain curve is the elastic modulus of the rock specimen. It can be seen that the slope of the stress-strain curve increases with the increase of confining pressure, which means that the elastic modulus is also gradually increasing. At the confining pressure of 5, 10, 15, and 20 MPa, the elastic modulus is 8.92, 10.03, 10.05, and 11.17 GPa, respectively.

3.2. Analysis of Deformation and Failure Characteristics. The macroscopic failure modes of red sandstone under different confining pressures are presented in Figure 4. At the confining pressure of 5 MPa, the failure presents shear mode. The failure starts from the upper left side of the rock and ends at the lower right side of the rock's bottom. When the confining pressure is 10 MPa, the main failure surface also shows shear failure. In addition to shear failure, the bottom corners are also damaged. This observation was regarded as one of the typical failure modes of the rock since the rock is a heterogeneous body with joints which will be fractured during the compression process. Due to the internal fissures, local small-scale cracking occurs at the bottom right end of the rock specimen. When the confining pressure is 15 MPa, the failure mode is similar to that of 5 MPa, but the shear inclination angle is reduced. At the confining pressure of 20 MPa, compared with other failure inclination angles, the failure surface inclination angle is the smallest. In summary, the failure mode of red sandstone with different confining pressures is dominated by the shear mode. As the confining pressure increases, the inclination of the failure surface decreases.

4. Numerical Modeling and Simulation Analysis

4.1. Numerical Model and Mesoparameter Calibration. The PFC^{3D} software was used to study the fracture development of red sandstone under different confining pressures, and the numerical models were established to simulate triaxial compression tests.

4.1.1. Numerical Model Construction. The PFC^{3D} simulation first generates a boundary wall according to the size of the rock specimen and then generates compact particles in the wall. By specifying the ratio of the maximum and minimum particle radius, the program can randomly generate a uniformly distributed particle model according to the preset maximum and minimum values. Figure 5 shows the constructed complete PFC^{3D} simulation test piece, which is basically consistent with that of the experimental specimen. The specimen size is 50 mm (diameter) × 100 mm (height), which consisted of 29,620 particles.

4.1.2. Homogenization Model. In order to make the particle size distribution of the generated model meet the specified requirements, the contact accuracy between particles must be high enough. This requires the overlap between adjacent particles in the particle system generated by the model generation algorithm is small enough. The particles are in close contact with the boundary and completely coupled. Therefore, to meet the above requirements, a self-programming
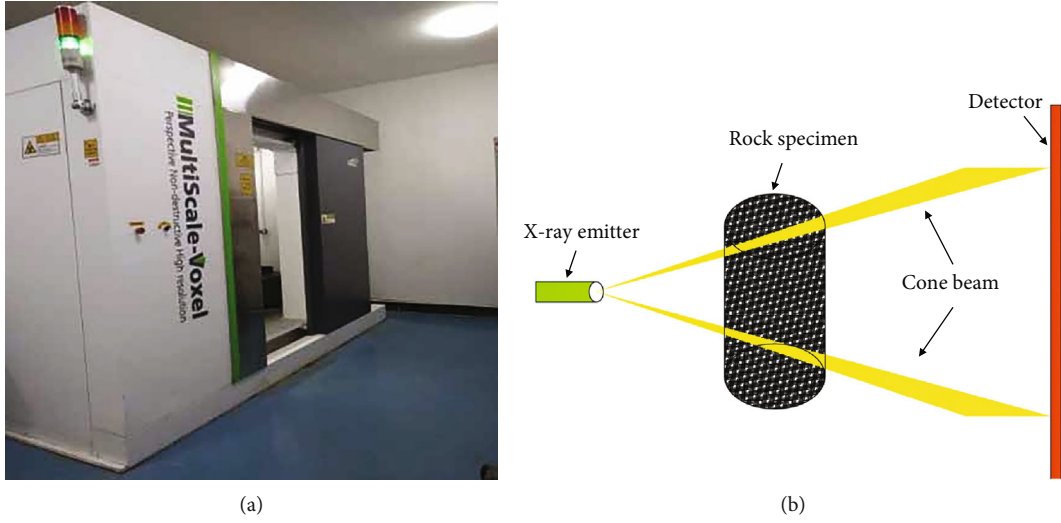
FIGURE 2: Microstructure test equipment: (a) CT scanner; (b) principles of CT scanning.

TABLE 1: Deformation parameters of the specimens under different confining pressures.

Sample number	Average density (g·cm^{-3})	Confining pressure (MPa)	Axial stress (MPa)	Elasticity modulus (GPa)	Poisson ratio	Cohesion (MPa)	Internal friction angle (°)
1		5	59.70	8.92	0.189		
2	2132	10	80.99	10.03	0.165	12.29	32.84
3		15	98.21	10.05	0.188		
4		20	110.12	11.17	0.189		

(a) Stress-strain curves under different confining pressures
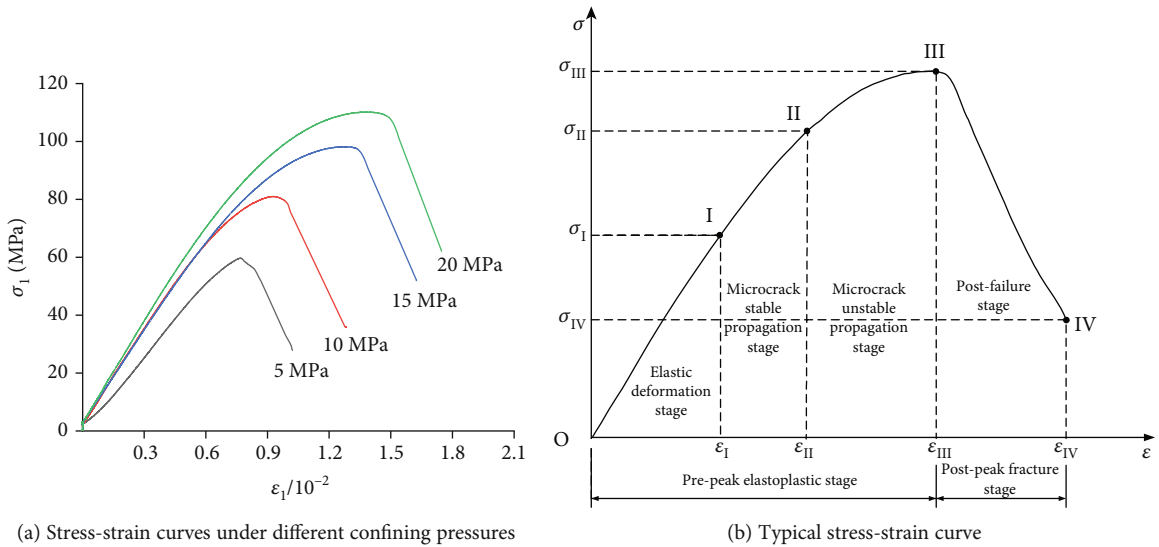

(b) Typical stress-strain curve

FIGURE 3: Stress-strain curves of red sandstone under different confining pressures.

capable of making the model close to the uniform state is proposed. Figure 6 shows the homogenization process. Through adjusting the model's boundary conditions, the contact between particles can reach the ideal state.

4.1.3. Calibration of Parameters. There are a variety of contact models in PFC^{3D}. Compared with other models,

the parallel bond model can transmit force and moment at the same time. Additionally, the stiffness after the failure of the parallel bond will decrease, which is similar to the plastic characteristics of the rock and better reflect the rock's mechanical characteristics. Therefore, the parallel bond model is chosen to calibrate the mesoparameters of the red sandstone [32–34]. Firstly, a set of mesoparameters are
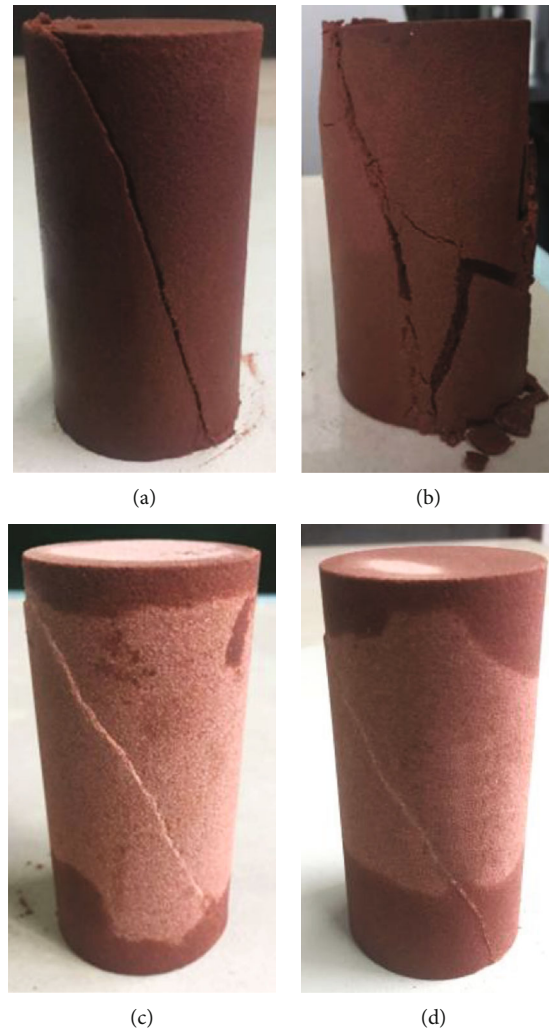
(a)   (b)

(c)   (d)

FIGURE 4: Macrofailures of red sandstone under different confining pressures: (a) 5 MPa; (b) 10 MPa; (c) 15 MPa; (d) 20 MPa.

assumed, and the stress-strain curves are obtained through the applying of the axial loads. Then, based on the measured data, the macroscopic compressive strength, the elastic modulus, and other macroscopic parameters are calculated and compared with the laboratory experiment. Finally, through continuously adjusting the mesoparameters, the stress-strain curve obtained by the numerical simulation test is consistent with the curve from the laboratory experiment, and the macroscopic damage is also similar to that observed in the laboratory experiments. A group of mesoparameters that are closest to the laboratory test are identified and applied to the numerical simulation test [35]. The mesoparameters are shown in Table 2.

4.2. Comparison of Test and Simulation. In the simulation test, the upper and lower walls simulate the indoor test loading stress, and the cylindrical wall is used to simulate the loading confining pressure. A self-compiled servo control program is used to control the wall motion. Through constantly updating the wall's speed, the wall contact force reaches the target confining pressure. After getting the target confining pressure, a constant loading rate to the upper and lower walls is applied. The wall exerts a constant loading rate to compress the model axially. Figure 7 shows the stress-strain curves of the intact red sandstone, and the final failure forms obtained through numerical simulation are shown in Figure 8.

In Figure 7, it was observed that the stress-strain curves under the triaxial compression simulated by PFC^{3D} were in good agreement with the results obtained in the laboratory tests. In the numerical simulation, for each 5 MPa increase in the confining pressure, the maximum axial stress obtained by the triaxial compression simulation is gradually increased, but the increased value of maximum axial stress is gradually reduced. Additionally, the slope of the curve in the elastic stage which is elastic modulus is increasing. When the confining pressure is 5 MPa, the maximum axial stress obtained by simulation is 59.27 MPa, and the elastic modulus is 9.04 GPa. The discrepancies of peak stress and elastic modulus between the simulation and lab test are 0.72% and 1.35%. At the confining pressures of 10, 15, and 20 MPa, the deviations of peak stress between simulations and laboratory experiments are 3.33%, 5.06%, and 1.33%, and the deviations of elastic modulus are 1.99%, 1.59%, and 6.98%. According to
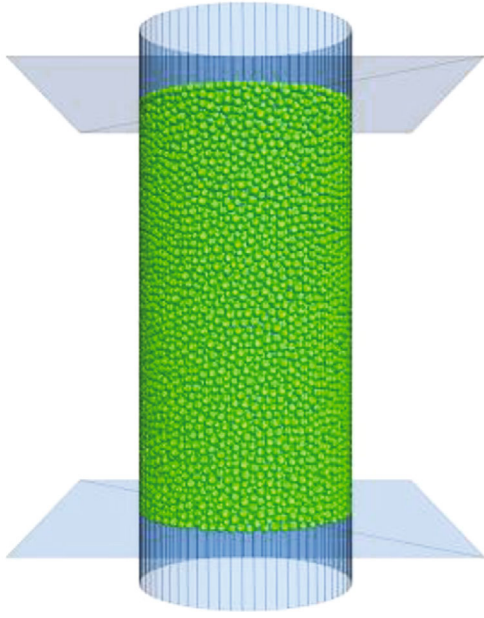
Figure 5: The PFC^{3D} model of standard triaxial compression specimen.

the Mohr-Coulomb criterion, the macroscopic mechanical parameters of the simulation experiment can be obtained. The cohesion force is 12.21 MPa, and the internal friction angle is 32.05°. The deviations from the indoor tests are 0.65% and 2.41%, respectively. These deviations are within a reasonable range, indicating that the numerical simulation results are accurate.

Figure 8 shows the fracture characteristics of the specimens under different confining pressures. The green particles represent the areas not broken, and the particles of other colors represent the broken area. The reason for this different color is that different fragments are formed after the fracture of the rock specimen penetrates, and the PFC^{3D} renders in different colors are to make the fracture more intuitive.

The particle failure can clearly show the macroscopic failure of the rock. The failure mainly presents the characteristics of shear failure, and the failure angle obtained by the simulation is basically the same as the real rock failure angle. As the confining pressure increases, the angle between the macroscopic crack of the rock and the horizontal plane is gradually decreasing, and the length of the crack is also decreasing. When the confining pressure is 5 MPa, the particles are affected by the hoop pressure. The damage appears to be shear failure, which is consistent with the failure mode of the test. As the confining pressure increases, the lateral pressure to the particles gradually increases, and the influence of lateral expansion deformation is gradually clear. The rock specimen gradually develops from the failure area of the loading interface to the middle area. The inclination angle of the failure surface also gradually decreases.

4.3. The Propagation Mode of Internal Fissures. The triaxial compression test is a method to study the mechanical behavior and failure mode of rock specimens, but these works have certain limitations. Triaxial tests can only

observe the distribution of cracks on the surface of the rock specimen. The distribution of internal cracks and the path of failure penetration are unclear. The emergence of numerical simulation will solve this problem. The slice function in the numerical simulation can be used to study the distribution of cracks and failure paths in the rock specimen, but there are still doubts about its accuracy. Here, a CT scan is proposed to verify the accuracy of the numerical simulation.

In order to observe the expansion of the internal fractures in the rock more accurately, the reconstructed 3D rock model was sectioned by using the AVIZO software. To observe the internal fracture paths, the failed specimens were cut three times along the axial direction. The location of each cutting is presented in Figure 9.

Figure 10 shows the comparison of the internal fracture mode of red sandstone between the test and simulation under a confining pressure of 15 MPa. In Figure 10, it was observed that the internal fracture behavior of the specimen obtained by numerical simulation is consistent with the CT results. At the slice of Cut 1, there is only one main crack in the numerical simulation. In addition to a main oblique shear crack on the CT image, a small shear crack is observed at the top of the red sandstone. This difference is that the red sandstone in its natural state has microcracks, while the numerical simulation is a homogenization model without microcracks. At the slice of Cut 2, the CT oblique shear main crack moves compared to the main crack observed at Cut 1. The upper rupture line moves up, and the lower rupture line moves down. The rupture angle becomes larger and longer. The numerical simulation appears with the same change, and the position of the main fracture surface also moves upward. At the slice of Cut 3, compared with Cut 2, the rupture line at the lower end of the oblique shear main crack shifts up. The failure angle becomes smaller, and the starting line becomes shorter, which is consistent with the main crack position shown by the numerical simulation. Comparing the CT results with the simulation results, the internal fracture behavior of the red sandstone obtained by the numerical simulation PFC^{3D} is consistent with the experimental results.

4.4. Crack Propagation Process. As shown in the above comparison, the results obtained from the laboratory test and numerical simulation are in good agreement. Numerical simulation can be used to observe the interior of the fracture process of rock specimens as compared to the laboratory test. Therefore, the inside crack evolution process is studied according to the simulation model of red sandstone under different confining pressures. Figure 11 shows the internal crack propagation process and crack changes of red sandstone under different confining pressure conditions, and Figure 12 gives the evolution of the number of microcracks in rocks under different conditions. In Figure 12, the characteristic points are selected to evaluate the crack evolution. Point I is generally selected at 2/5 of the peak stress. Point II is the transition from the elastic stage to the plastic stage, which is generally considered to be about 2/3 of the peak strength [36, 37]. Therefore, the selected characteristic points are 2/5 peak stress, 2/3 peak stress, the peak stress, and failure stress.
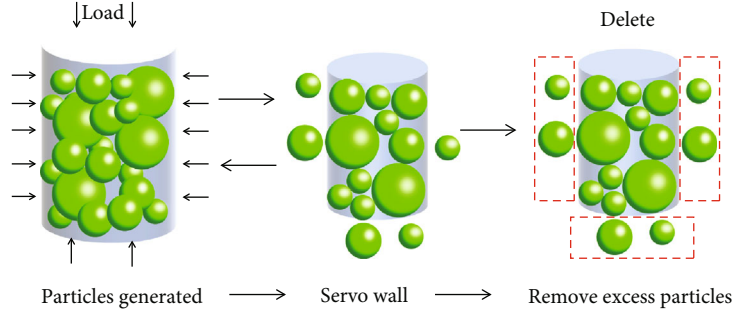
Figure 6: Homogenization process of the model.

Table 2: Mesoparameter calibration of numerical simulation.

Microparameters	Values
The minimum radium of the ball, R_{min}/mm	0.85
Ratio of the maximum to the minimum radium of the ball, R_{max}/R_{min}	1.5
Density of the ball, ρ/(kg/m^3)	2132
Ball friction coefficient, μ	0.5
Young's modulus of the ball, E_C/GPa	9.2
Ratio of normal to shear stiffness of the ball, k_n/k_s	2.3
Radius multiplier of the parallel bond, λ	1.0
Young's modulus of the parallel bond, $\bar{E}_C$/GPa	9.2
Ratio of normal to shear stiffness of the parallel bond, $\bar{k}_n/\bar{k}_s$	2.3
Normal strength of the parallel bond, σ/MPa	32.5
Shear strength of the parallel bond, c/MPa	32.5
Friction angle of the parallel bond, φ/°	30

Figure 7: Numerical simulation curves of stress-strain.

Under the confining pressure of 5 MPa, the simulated crack propagation process of the red sandstone specimen is shown in Figure 11(a), and the corresponding curve of the number of cracks is shown in Figure 12(a). In the process of simulating the fracture of red sandstone, no microcracks were generated at point I (σ_1 = 23.71 MPa), which is consistent with the theory of microcracks in the experiment. When the axial stress increases to point II (σ_1 = 39.51 MPa accounts for 2/3 of the peak stress), the microcracks begin to occur at the end of the rock specimen. The number of microcracks is 72, accounting for about 1.22% of the total number of microcracks at peak point III. With the increase of the axial stress, the axial deformation continues to increase. Before the axial stress reaching point III (σ_1 = 59.27 MPa), the specimen is at the stage of plastic deformation where new microcracks initiate. In this stage, the cracks began to expand; the number of microcracks is up to 5910. Additionally, an oblique shear failure crack was being formed. After reaching the peak stress, the axial stress began to decline, and the specimen was completely destroyed at point IV (σ_1 = 42.10 MPa). At point IV, a macroscopic oblique
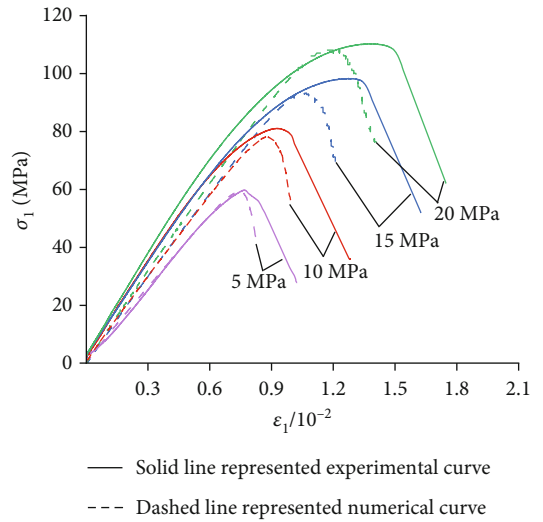
shear failure formed, with a rapid increase in the number of microcracks. The number of microcracks eventually reached 21700.

Figure 11(b) shows the simulated crack propagation process of the red sandstone specimen at the confining pressure of 10 MPa, and Figure 12(b) shows the corresponding curve of microcrack quantity. The cracking process is consistent with that of 5 MPa. When the axial strain is 0.319×10^{-2} (point I), no cracks occur. As the axial strain increases to 0.537×10^{-2} (point II), 123 microcracks are generated at the end of the rock, accounting for about 2.01% of the total number of microcracks at peak point III. With the continuous increase of strain, the direction of crack propagation is determined in the elastic-plastic region, and it can be clearly observed that the microcracks form an oblique shear crack. At this time, the number of microcracks is 6110. After point III, the specimen steps into the stage of microcrack penetration failure. The number of microcracks continues to increase until the axial strain reaches point IV. At this point, the rock specimen is completely destroyed, and the final number of microcracks reaches 23,100. It is observed that the microcracks interact with each other forming an oblique shear macrocrack. Figures 11(c) and 11(d) are the crack propagation process of red sandstone under confining
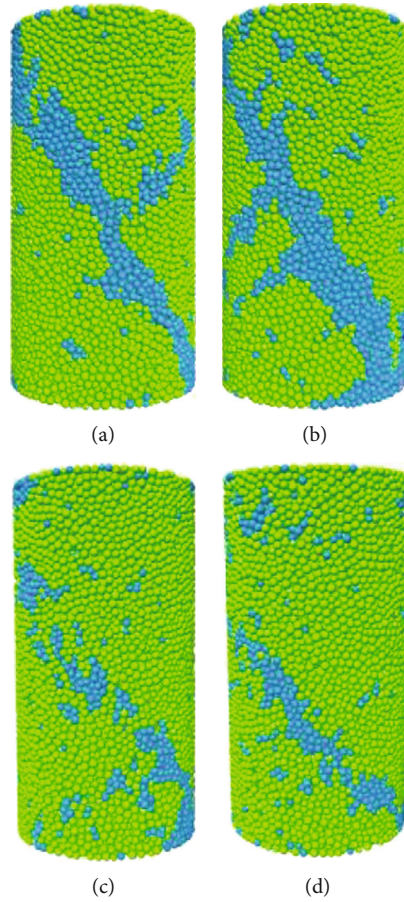
(a)   (b)

(c)   (d)

FIGURE 8: Macroscopic failure modes of redstone under different confining pressure by PFC^{3D}: (a) 5 MPa; (b) 10 MPa; (c) 15 MPa; (d) 20 MPa.

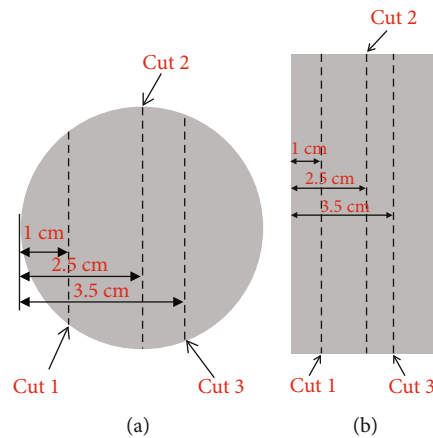(a)   (b)

FIGURE 9: Locations of the cuttings: (a) cross-section; (b) longitudinal section.

pressures 15 and 20 MPa, and Figures 12(c) and 12(d) show the corresponding curve of microcrack quantity. The initiation, propagation, and interaction of crack in the specimens are consistent with that of 5 MPa. The cracks also start from the end position of specimen and propagate obliquely under the combined action of axial force and confining pressure. The macroscopic oblique shear failure is eventually formed.

5. Analysis of Experiment and Simulation Results

5.1. Strength Characteristics and Failure Modes.
The laboratorial triaxial experiment found that the triaxial compression deformation of red sandstone has elastic deformation stage, microcrack stable propagation stage, microcrack unstable

Cut 1 (1cm) Cut 2 (2.5 cm) Cut 3 (3.5 cm) Cut 1 (1cm) Cut 2 (2.5 cm) Cut 3 (3.5 cm)
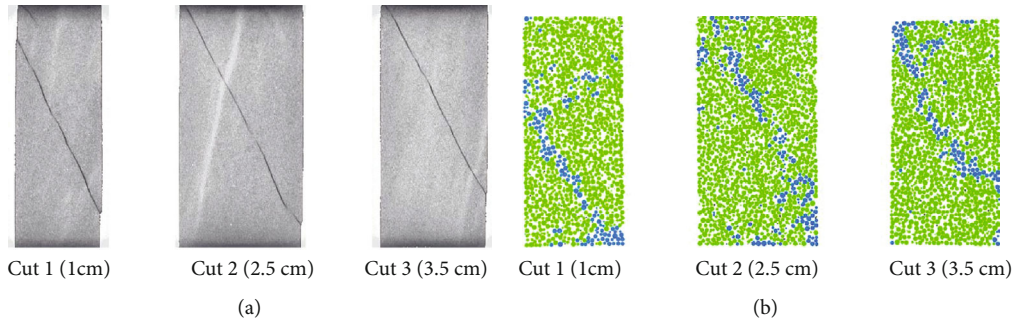
(a) (b)

Figure 10: Comparison of internal fractures in red sandstone under 15 MPa: (a) CT scan; (b) simulation.
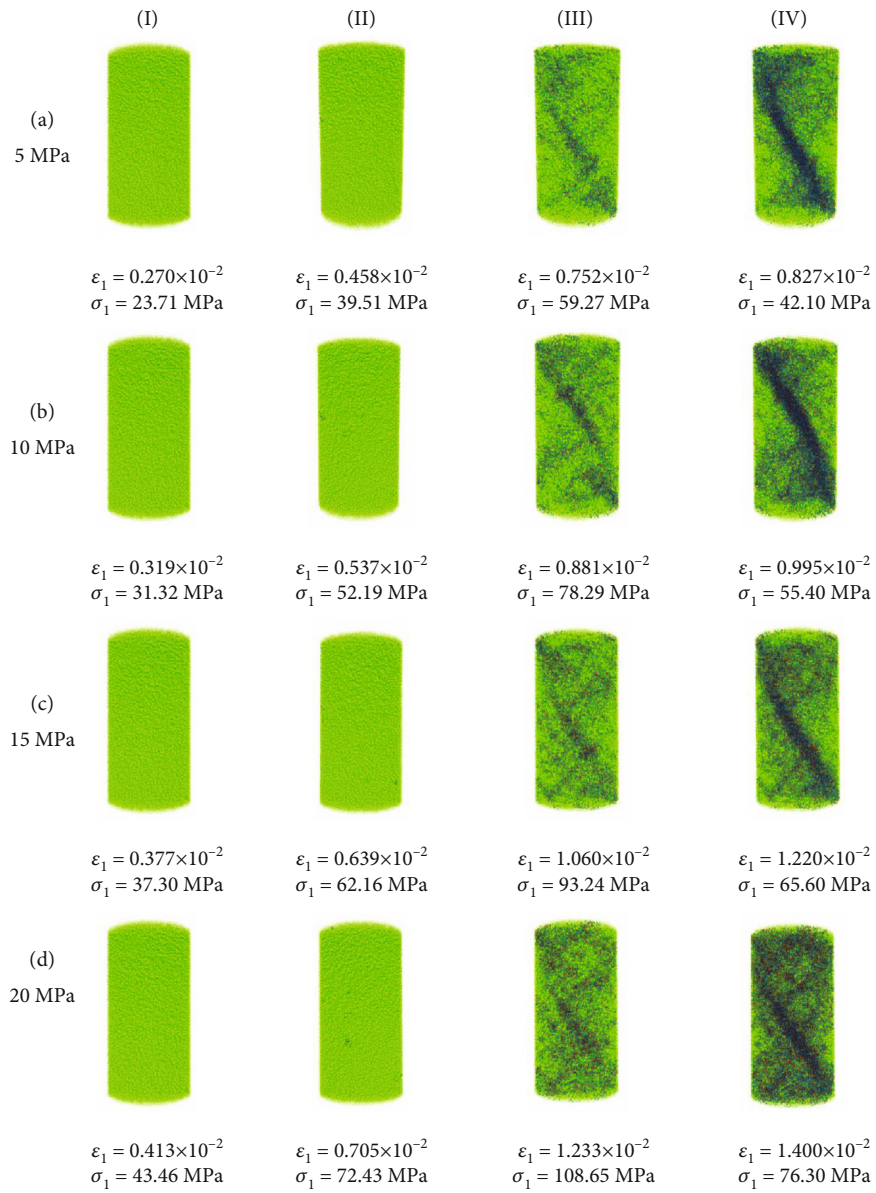

Figure 11: Internal crack propagation rules of red sandstone under different confining pressure conditions.
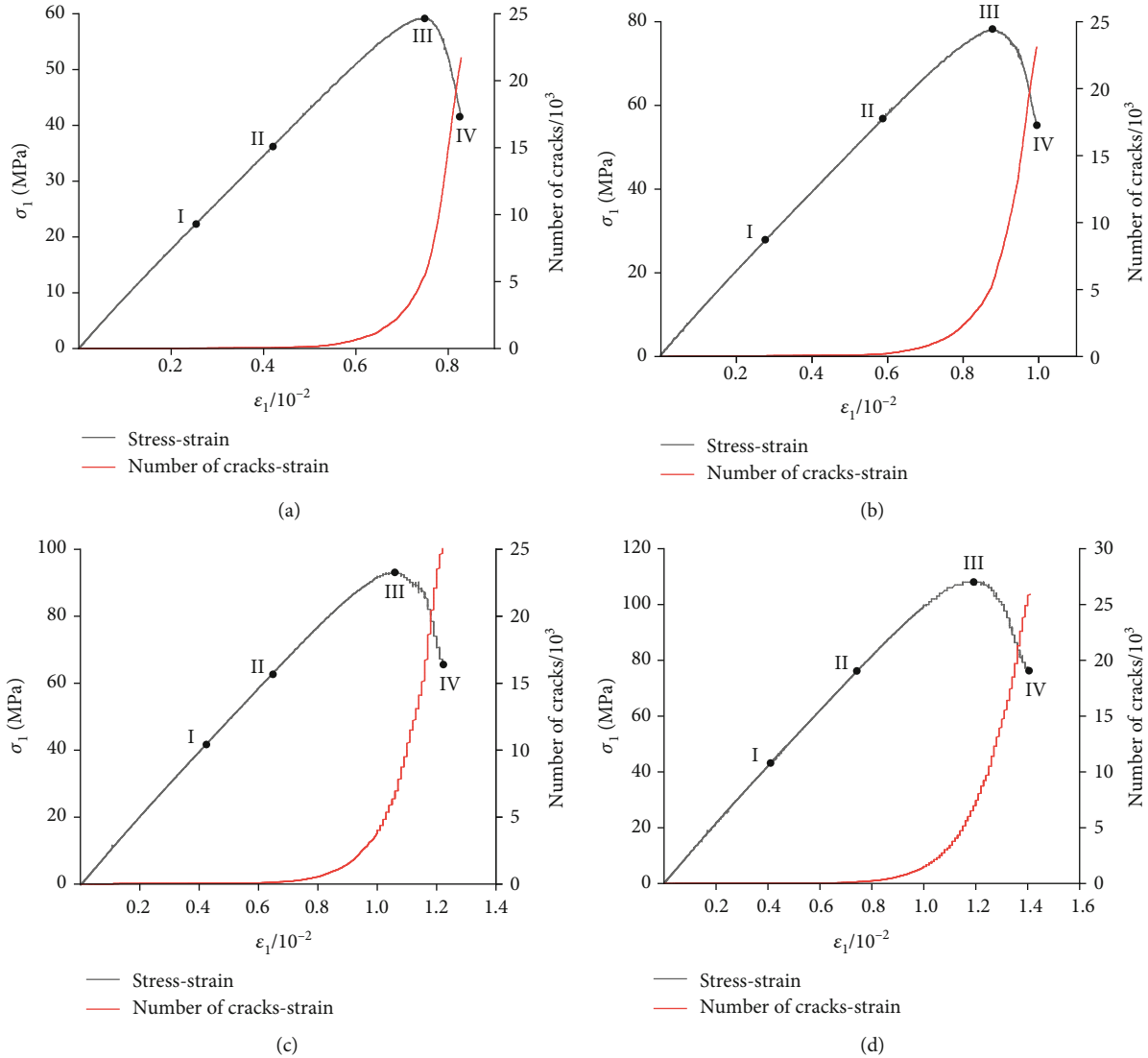
(a)

(b)

(c)

(d)

FIGURE 12: The number of microcracks in red sandstone under different confining pressure conditions: (a) 5 MPa; (b) 10 MPa; (c) 15 MPa; (d) 20 MPa.

propagation stage, and postfailure stage. For the model established by the numerical simulation, the deformations and failures are consistent with the laboratorial test. From the triaxial test and PFC^{3D} simulations, it can be seen that the red sandstone failed in the shear mode. The peak strength, elastic modulus, peak strain, and residual stress of red sandstone increase while the inclination of the failure surface decreases as the confining pressure increases. This indicates that the increase of confining pressure can improve the anti-destructive ability of red sandstone to a certain extent, in other words, playing a certain protective effect on the deformation and failure of red sandstone.

5.2. Comparative Analysis of Numerical Simulation. From the rock failure characteristics obtained by the PFC^{3D} simulation, it is observed that the three-dimensional numerical simulation can accurately simulate the macro- and microfailure mode of the rock under pressure. In laboratory

experiments, the macroscopic failure of red sandstone under different confining pressures all showed oblique shear failure, and the failure angle decreased with the increase of confining pressure. Simulations of red sandstone under different confining pressures are consistent with the laboratorial experiments, with only a few differences on the tiny crack. This is because the rock itself has cracks in nature, which have an influence to rock damage in the laboratorial experiment. The homogeneous model was established by the method of numerical simulation that leads to the slight differences between numerical simulation and experimental results.

The PFC^{3D} homogenization simulation can not only simulate the changes of macroscopic cracks but also analyze the development of its internal cracks. By comparing internal cracks from the CT three-dimensional reconstruction of red sandstone with numerical simulation results under confining pressure of 15 MPa, it is clear that the shape of

the main failure cracks inside the simulated rock specimen is consistent with the internal cracks of the real rock specimen. The good agreement of the results obtained from the numerical simulation and the CT scanning indicates that the numerical simulation is accurate for the distribution of cracks in the red sandstone and the path of penetration failure.

The PFC^{3D} homogenization simulation can obtain the fracture process of the rock specimen under the condition of triaxial compression and reveal the evolution law of microcracks in the rock specimen. In the initial stage, the number of microcracks is very small. In the elastic-plastic deformation stage, the cracks begin to be active and the number of cracks begins to increase. Compared with the first two stages, the number of cracks increases exponentially after the peak stress. It indicates that the microcracks of the rock specimen interact and form the macrocracks at this stage. In addition, it is found that the microcrack propagation mode of red sandstone under different confining pressures is basically the same. The microcracks in red sandstone start from the end of the rock specimen and gradually form oblique shear failure under the action of external force. The consistencies of the mechanical parameters and fracture evolution processes of the red sandstone obtained from numerical simulation and the indoor experiment also confirmed the feasibilities of using the PFC^{3D} numerical simulation to study rock failure.

6. Conclusion

In this study, with the applications of indoor triaxial compression tests, PFC^{3D} numerical simulation, and CT scanning technique, the internal and external deformation and failure characteristics of red sandstone under different confining pressures were analyzed at micro- and macroscales. The following conclusions were obtained:

(1) The effects of confining pressure on the mechanical properties and failure characteristics of red sandstone are very obvious. The failure surface of the specimens shows shear modes. As the confining pressure increases, the peak stress, elastic modulus, and peak strain of the rock increase, while the inclination angles of the shear surface decrease

(2) The process of crack initiation and propagation was studied using the PFC^{3D} numerical simulation and CT scanning. The cracks first began to occur at the end, propagated obliquely with the action of axial stress and confining pressure producing a large number of the microcracks, and finally, microcracks interact with each other forming the macrocracks and resulted in oblique shear failure

(3) The mechanical parameters, fracture evolution processes, and macro/microfracture characteristics of the specimens obtained from PFC^{3D} numerical simulation and the CT three-dimensional reconstruction are consistent. The consistencies confirmed that PFC^{3D} can simulate mechanical properties and the failure characteristics of red sandstone under differ-

ent confining pressures, providing a feasible numerical method for studying the mechanical behavior of rock. In addition, this method can also be used to study the internal micromechanism of the rock failure and provide a theoretical basis for rock strength prediction and safety evaluation under loads

Data Availability

The detailed data used to support the findings of this study are available from the corresponding author upon request.

Conflicts of Interest

The authors declare that they have no conflicts of interest.

Acknowledgments

References

[1] Y. Wang, X. Zhou, and Y. Shou, "The modeling of crack propagation and coalescence in rocks under uniaxial compression using the novel conjugated bond-based peridynamics," *International Journal of Mechanical Sciences*, vol. 128, pp. 614–643, 2017.

[2] V. Sarfarazi and H. Haeri, "A review of experimental and numerical investigations about crack propagation," *Computers and Concrete*, vol. 18, no. 2, pp. 235–266, 2016.

[3] J. J. Chen, P. Liu, H. B. Zhao, and C. Zhang, "Analytical studying the axial performance of fully encapsulated rock bolts," *Engineering Failure Analysis*, vol. 128, article 105580, 2021.

[4] S. S. Wu, H. L. Ramandi, H. Chen, A. Crosky, P. Hagan, and S. Saydam, "Mineralogically influenced stress corrosion cracking of rockbolts and cable bolts in underground mines," *International Journal of Rock Mechanics and Mining Sciences*, vol. 119, pp. 109–116, 2019.

[5] S. S. Wu, X. H. Zhang, J. P. Li, and Z. Wang, "Investigation for influences of seepage on mechanical properties of rocks using acoustic emission technique," *Geofluids*, vol. 1155, 19 pages, 2020.

[6] S. Xie, H. Lin, Y. Wang et al., "Nonlinear shear constitutive model for peak shear-type joints based on improved Harris damage function," *Archives of Civil and Mechanical Engineering*, vol. 95, 2020.

[7] H. Lin, X. Zhang, Y. Wang et al., "Improved nonlinear Nishihara shear creep model with variable parameters for rock-like materials," *Advances in Civil Engineering*, vol. 2020, Article ID 7302141, 15 pages, 2020.

[8] Y. L. Zhao and L. Y. Zhang, "Experimental study on the mud-water inrush characteristics through rock fractures," *Advances in Civil Engineering*, vol. 2018, Article ID 2060974, 7 pages, 2018.

[9] C. Y. Zhang, C. Z. Pu, R. H. Cao, T. T. Jiang, and G. Huang, "The stability and roof-support optimization of roadways passing through unfavorable geological bodies using advanced detection and monitoring methods, among others, in the

Sanmenxia Bauxite Mine in China's Henan Province," *Bulletin of Engineering Geology and the Environment*, vol. 78, no. 7, pp. 5087–5099, 2019.

[10] X. Liu, L. Wu, Y. Zhang, S. Wang, X. Yao, and X. Wu, "The characteristics of crack existence and development during rock shear fracturing evolution," *Bulletin of Engineering Geology and the Environment*, vol. 80, pp. 1671–1682, 2021.

[11] J. L. Liu, Y. H. Liu, Y. J. Zhu et al., "Study of influences of rock hardness on crack evolution rule under hydraulic fracturing," *IOP Conference Series Earth and Environmental Science*, vol. 558, no. 3, article 032003, 2020.

[12] Y. Bai, R. L. Shan, Y. Ju et al., "Experimental study on the strength, deformation and crack evolution behaviour of red sandstone samples containing two ice-filled fissures under triaxial compression," *Cold Regions Science and Technology*, vol. 174, article 103061, 2020.

[13] S. Q. Yang, Y. Z. Jiang, W. Y. Xu, and X. Q. Chen, "Experimental investigation on strength and failure behavior of pre-cracked marble under conventional triaxial compression," *International Journal of Solids and Structures*, vol. 45, no. 17, pp. 4796–4819, 2008.

[14] C. Y. Zhang, Y. X. Wang, and T. T. Jiang, "The propagation mechanism of an oblique straight crack in a rock sample and the effect of osmotic pressure under in-plane biaxial compression," *Arabian Journal of Geosciences*, vol. 13, no. 15, pp. 736–751, 2020.

[15] S. Wu, J. Li, J. Guo, G. Shi, Q. Gu, and C. Lu, "Stress corrosion cracking fracture mechanism of cold-drawn high-carbon cable bolts," *Materials Science and Engineering: A*, vol. 769, article 138479, 2020.

[16] H. Mokhtarian, H. Moomivand, and H. M. Moomivand, "Effect of infill material of discontinuities on the failure criterion of rock under triaxial compressive stresses," *Theoretical and Applied Fracture Mechanics*, vol. 108, article 102652, 2020.

[17] S. Q. Yang, H. W. Jing, and S. Y. Wang, "Experimental investigation on the strength, deformability, failure behavior and acoustic emission locations of red sandstone under triaxial compression," *Rock Mechanics and Rock Engineering*, vol. 45, no. 4, pp. 583–606, 2012.

[18] X. Ma, G. L. Wang, D. W. Hu, Y. Liu, H. Zhou, and F. Liu, "Mechanical properties of granite under real-time high temperature and three- dimensional stress," *International Journal of Rock Mechanics and Mining Sciences*, vol. 136, no. 1, article 104521, 2020.

[19] Y. D. Jiang, X. F. Xian, and J. Xu, "A research on sandstone uniaxial and triaxial compression tests," *China Mining Magazine*, vol. 13, no. 4, pp. 66–69, 2004.

[20] H. Kawakata, A. Cho, T. Kiyama, T. Yanagidani, K. Kusunose, and M. Shimada, "Three-dimensional observations of faulting process in Westerly granite under uniaxial and triaxial conditions by X-ray CT scan," *Tectonophysics*, vol. 313, no. 3, pp. 293–305, 1999.

[21] P. Christe, P. Turberg, V. Labiouse, R. Meuli, and A. Parriaux, "An X-ray computed tomography-based index to characterize the quality of cataclastic carbonate rock samples," *Engineering Geology*, vol. 117, no. 3-4, pp. 180–188, 2011.

[22] S. Q. Yang, P. F. Yin, Y. H. Huang, and J. L. Cheng, "Strength, deformability and X-ray micro-CT observations of transversely isotropic composite rock under different confining pressures," *Engineering Fracture Mechanics*, vol. 214, pp. 1–20, 2019.

[23] J. B. Zhu, T. Zhou, Z. Y. Liao, L. Sun, X. B. Li, and R. Chen, "Replication of internal defects and investigation of mechanical and fracture behaviour of rock using 3D printing and 3D numerical methods in combination with X-ray computerized tomography," *International Journal of Rock Mechanics and Mining Sciences*, vol. 106, pp. 198–212, 2018.

[24] X. P. Zhou, Y. X. Zhang, and Q. L. Ha, "Real-time computerized tomography (CT) experiments on limestone damage evolution during unloading," *Theoretical and Applied Fracture Mechanics*, vol. 50, no. 1, pp. 49–56, 2008.

[25] C. Zhang, H. Lin, C. Qiu, T. Jiang, and J. Zhang, "The effect of cross-section shape on deformation, damage and failure of rock-like materials under uniaxial compression from both a macro and micro viewpoint," *International Journal of Damage Mechanics*, vol. 29, no. 7, pp. 1076–1099, 2020.

[26] B. Gong, Y. J. Jiang, and L. J. Chen, "Feasibility investigation of the mechanical behavior of methane hydrate- bearing specimens using the multiple failure method," *Journal of Natural Gas Science and Engineering*, vol. 69, article 102915, 2019.

[27] X. Fan, K. H. Li, H. P. Lai, Y. Xie, R. Cao, and J. Zheng, "Internal stress distribution and cracking around flaws and openings of rock block under uniaxial compression: a particle mechanics approach," *Computers and Geotechnics*, vol. 102, pp. 28–38, 2018.

[28] T. H. Wu, Y. T. Gao, Y. Zhou, and J. W. Li, "Experimental and numerical study on the interaction between holes and fissures in rock-like materials under uniaxial compression," *Theoretical and Applied Fracture Mechanics*, vol. 106, article 102488, 2020.

[29] X.-P. Zhang and L. N. Y. Wong, "Cracking processes in rock-like material containing a single flaw under uniaxial compression: a numerical study based on parallel bonded-particle model approach," *Rock Mechanics and Rock Engineering*, vol. 45, no. 5, pp. 711–737, 2011.

[30] X. Yang, Z. P. You, Z. G. Wang, and Q. L. Dai, "Review on heterogeneous model reconstruction of stone-based composites in numerical simulation," *Construction and Building Materials*, vol. 117, pp. 229–243, 2016.

[31] Y. F. Zhao, *Stress-induced permeability evolution in coal: laboratory testing and numerical simulations, [PhD thesis]*, Technischen Universität Bergakademie Freiberg, Germany, 2020.

[32] N. Cho, C. D. Martin, and D. C. Sego, "A clumped particle model for rock," *International Journal of Rock Mechanics and Mining Sciences*, vol. 44, no. 7, pp. 997–1010, 2007.

[33] L. Cheung, C. O'Sullivan, and M. R. Coop, "Discrete element method simulations of analogue reservoir sandstones," *International Journal of Rock Mechanics and Mining Sciences*, vol. 63, pp. 93–103, 2013.

[34] J. M. Xu, Z. L. Xie, and H. T. Jia, "Simulation of mesomechanical properties of limestone using particle flow code," *Rock and Soil Mechanics*, vol. 31, no. 2, pp. 390–395, 2010.

[35] B. Gong, Y. J. Jiang, P. Yan, and S. H. Zhang, "Discrete element numerical simulation of mechanical properties of methane hydrate-bearing specimen considering deposit angles," *Journal of Natural Gas Science and Engineering*, vol. 76, article 103182, 2020.

[36] R. E. Goodman, *Introduction to Rock Mechanics*, Wiley, Canada, 1989.

[37] M. F. Cai, M. C. He, and D. Y. Liu, *Rock Mechanics and Engineering*, Beijing Publishing House, China, 2013.